Chemical Engineering Journal 525 (2025) 170471

Contents lists available at ScienceDirect

Chemical Engineering Journal

journal homepage: www.elsevier.com/locate/cej

# Optimization of NiHCF/$MnO_2$ composite electrodes for lithium extraction via capacitive deionization: A case of core-shell construction strategy

Yang Bao [a,1,2], Shijun Miao [a,1], Pengcheng Yin [a], Dawei Li [a], Feihu Li [a,b,*]

[a] Collaborative Innovation Center of Atmospheric Environment and Equipment Technology, Jiangsu Key Laboratory of Atmospheric Environment Monitoring and Pollution Control, School of Environmental Science and Engineering, Nanjing University of Information Science and Technology, 219 Ningliu Road, Nanjing 210044, China

[b] NUIST Reading Academy, Nanjing University of Information Science and Technology, 219 Ningliu Road, Nanjing 210044, China

ARTICLE INFO

*Keywords:*
Electrochemical lithium extraction
Capacitive deionization
Prussian blue analogs
Manganese oxide
Core-shell construction
Salar brine

ABSTRACT

The rapid growth of lithium (Li) ion batteries, particularly in electric vehicles (EVs) and large-scale energy storage facilities, has catalyzed an ever-increasing demand for Li. Current Li mining from brines based on evaporation-precipitation is time-consuming and water-intensive. Here, we report three NiHCF/$MnO_2$ composite electrodes based on core-shell construction strategies for $Li^+$ extraction from brine on a rocking-chair capacitive deionization (RCDI) platform. We find that the $MnO_2$ components varied with the composing condition from α-, δ- to λ-$MnO_2$ and that the core-shell structured NiHCF@λ-$MnO_2$ electrode showed the optimal ion migration rate, highest specific capacity, and the best cycling stability. Notably, we reveal that the NiHCF@λ-$MnO_2$ electrode presented the optimum $Li^+$ extraction performance with respect to adsorption capacity, adsorption rate, and energy consumption (e.g., achieving the highest $Li^+$ capacity of 43.51 mg $Li^+$ $g^{-1}$ with a rate of 8.1 mg $g^{-1}$ $min^{-1}$, and at an energy cost of 0.86 Wh $g^{-1}$ in 20 mM LiCl solution at 1.2 V). In addition, we demonstrate that the NiHCF@λ-$MnO_2$ electrode maintained high cycling stability over 40 consecutive cycles of $Li^+$ intercalation/deintercalation, with 78.4 % capacity retention in 10 mM of LiCl solution. Importantly, the NiHCF@λ-$MnO_2$ electrode also provided excellent $Li^+$ selectivity in both the synthetic brine and the actual brine from the East Taijinaier Salt Lake, with exceptional separation factors as high as 68.7 and 21.0 for $Li^+$ against $Na^+$ and $Mg^{2+}$ ions, respectively. Such unparalleled selectivity is believed to be attributed to the combination of structural and charge synergy of the NiHCF@λ-$MnO_2$ composite. Our study highlights that a rational core-shell construction strategy can boost the optimal integration of NiHCF and $MnO_2$, thus leveraging their potential to preferentially extract $Li^+$ from brines.

## 1. Introduction

Lithium (Li), known as 'green energy metal' or 'white oil', is a critical element for global green energy and strategic emerging industries [1]. It has been extensively used in a wide range of areas, such as batteries (e.g., Li-ion batteries, LIBs), ceramics, pharmaceuticals, nuclear fusion, lubricants, and the polymers industries [2,3]. The rapid growth of LIBs for electric vehicles (EVs) and large-scale energy storage facilities has provoked an ever-increasing demand for lithium [4,5]. However, current lithium mining from hard rocks (e.g., spodumene ore) is usually energy-intensive with a high carbon footprint and yields large volumes of waste rock and acid [6], while salar brine extraction based on evaporation-precipitation is time-consuming (i.e., 1–2 years for evaporation) and water-intensive, accompanied by many environmental concerns to local ecosystems [1]. In the context of global carbon neutrality, selective lithium extraction from seawater and salar brines is therefore very promising, as most lithium resources are found in seawater and salt lakes [1–3].

To date, many innovative strategies for direct lithium extraction (DLE) from seawater and salar brines such as solvent extraction [7],

* Corresponding author at: Collaborative Innovation Center of Atmospheric Environment and Equipment Technology, Jiangsu Key Laboratory of Atmospheric Environment Monitoring and Pollution Control, School of Environmental Science and Engineering, Nanjing University of Information Science and Technology, 219 Ningliu Road, Nanjing 210044, China.
*E-mail address:* fhli@nuist.edu.cn (F. Li).
[1] These authors contributed equally.
[2] Present address: College of Architecture and Environment, Sichuan University, Chengdu 610065, China

https://doi.org/10.1016/j.cej.2025.170471
Received 16 July 2025; Received in revised form 25 October 2025; Accepted 3 November 2025
Available online 4 November 2025

adsorption (e.g., lithium-ion sieve (LIS) adsorption) [8,9], membrane-based separation [10], and electrochemical extraction (e.g., electrodialysis) [4,5,8,11,12] have been extensively explored over the past decades. Of these technologies, electrochemical lithium extraction based on ion pumping, electrodialysis, and capacitive deionization (CDI) has been identified as an auspicious and bright strategy for Li extraction due to its unique properties, including high efficiency, environmental friendliness, operational simplicity, and cost-effectiveness [4,5,8,11,12]. For instance, CDI has been demonstrated as a high-performance platform for capturing Li ions from brines by integrating ion-exchange membranes inside the cells via various configurations, including membrane capacitive deionization (MCDI), hybrid capacitive deionization (HCDI), and flow-electrode capacitive deionization (FCDI) [13–17]. Materials such as activated carbon (AC), spinel lithium manganese oxide ($LiMn_2O_4$, LMO), lithium-manganese-titanium oxide, λ-$MnO_2$, $Li_3V_2(PO_4)_3$, $FePO_4$, and $LiFePO_4$ have been successfully used

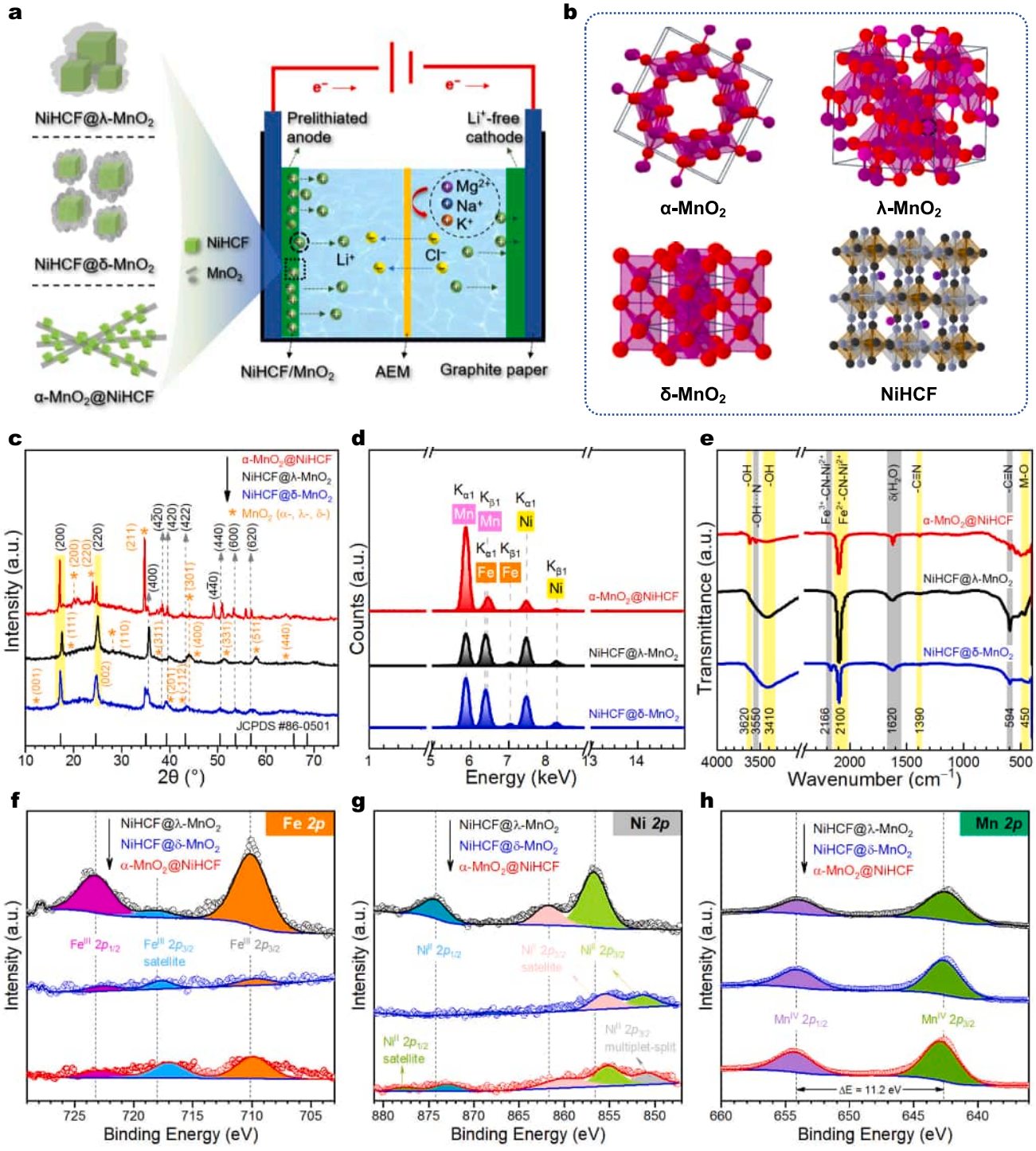


**Fig. 1.** (a) Schematical illustration of the electrolytic cell with NiHCF/$MnO_2$ composite as electrodes for lithium extraction; (b) the crystalline structure of each constituent constructing the NiHCF/$MnO_2$ composites (i.e., α-$MnO_2$ with 2 × 2 tunnels of size 4.6 Å × 4.6 Å, λ-$MnO_2$ with tunnel sizes of ~2.4–2.8 Å, δ-$MnO_2$ with an interlayer space of ~7 Å, and NiHCF with channels of size ~6.5 Å); (c) XRD patterns, (d) XRF, (e) FTIR, and (f-h) XPS spectra of the Fe 2p (f), Ni 2p (g) and Mn 2p (h) regions of the as-prepared NiHCF/$MnO_2$ composites (i.e., α-$MnO_2$@NiHCF, NiHCF@λ-$MnO_2$ and NiHCF@δ-$MnO_2$).

as electrodes due to their structural integrity and/or tailorability via various optimization strategies, and the intrinsic $Li^+$ preference [13–18]. Ideally, optimum electrodes should possess a high ion storage capacity, structural stability, and inherent lithium selectivity against other competitive ions. Therefore, the major challenge for CDI-based DLE technologies lies in the development of lithium extraction electrode materials with higher capacity and higher selectivity, particularly in complex brine matrices.

Recently, coupling lithium-ion sieves (LIS) adsorption with CDI has been demonstrated as an effective strategy for the selective extraction of lithium ions, as it can substantially improve $Li^+$ selectivity and adsorption capacity at low energy consumption, environmental impact, and operating costs [19,20]. The principle of selective uptake of $Li^+$ ions using LIS-based CDI relies on the property of LIS electrode materials assembled into a CDI cell, which acts as the $Li^+$ capturing arsenal when a certain electric field is applied between the two electrode plates. LIS materials are generally classified into i) spinel-type lithium manganese oxides, ii) layered lithium manganese oxides, iii) lithium titanium oxides, and iv) mixed metal oxides [21,22]. Of these LIS materials, Mn-based LISs, including λ-$MnO_2$ and LMO, have gained much attention [14,19–24]. A variety of strategies—lattice engineering, heterojunction/core-shell construction, and field regulation—have been extensively explored to leverage the $Li^+$ selectivity and adsorption capacity of LMO-based electrodes [23,24]. To improve the electrical conductivity of Mn-based LISs for CDI, carbon materials, including AC [25], graphite felt [26], carbon cloth [27], and carbon nanotubes (CNTs) [28], have been widely adopted as a scaffold based on an interface engineering strategy. However, integrating $MnO_2$ with carbon matrices introduces several technical and operational challenges, including electrode performance fading at higher $MnO_2$ loading, weakening of $Li^+$ selectivity, reducing Coulombic efficiency, and lowering $MnO_2$'s active sites [29,30], which may limit their practical application.

Notably, core-shell construction strategies have emerged as a promising approach for developing high-performance composite electrodes for CDI or supercapacitors [31,32]. For instance, a core-shell structured RA-$LiMn_2O_4$ material with rutile-anatase (RA) as the shell and spinel $LiMn_2O_4$ as the core appeared to display enhanced stability [32]. As a well-known Faradaic material with a stable and open framework for rapid ion conduction, Prussian blue analogs (PBAs) have been extensively explored as CDI electrodes (e.g., nickel hexacyanoferrate, NiHCF) [33], but have yet to be fully inspected for the selective $Li^+$ capture [5,12]. The integration of $MnO_2$ with PBA for composite electrodes has not yet been examined for lithium extraction from brines. To this end, we explore the optimal integration of NiHCF/$MnO_2$ composites based on core-shell construction strategies with NiHCF and $MnO_2$ alternating as core or shell layer for improving lithium extraction from brines (Fig. 1a). Our study focuses on the experimental demonstration of a hypothesis of combination of NiHCF and $MnO_2$ for the selective $Li^+$ capture, prior experimental and density functional theory (DFT) studies [34] have established that both $MnO_2$ and the NiHCF's framework favors $Li^+$ diffusion due to their inherent pore diameters greater than $Li^+$ (~0.76 Å) (Fig. 1b). Three core-shell structured NiHCF/$MnO_2$ composites (i.e., α-$MnO_2$@NiHCF, NiHCF@λ-$MnO_2$ and NiHCF@δ-$MnO_2$) were prepared following various wet-chemistry approaches and fully characterized for their physicochemical and electrochemical properties. We demonstrated that the NiHCF@λ-$MnO_2$ electrode demonstrated the optimum $Li^+$ extraction performance with respect to adsorption capacity, adsorption rate, and energy consumption. The electrochemical cycling performance and $Li^+$ selectivity were then evaluated for the NiHCF@λ-$MnO_2$ electrode in both the synthetic and the actual brines from East Taijinaier Salt Lake. Overall, our results provide a new perspective for the optimized design of CDI electrodes for $Li^+$ extraction from brines.

## 2. Experimental section

All chemicals were purchased from Aladdin Scientific Co. (Shanghai, China) unless otherwise specified, and are of reagent grade or above. All solutions used in this study were prepared using deionized water (DI $H_2O$) with resistivity ≥18 MΩ·cm at 25 °C.

### 2.1. Synthesis and characterization of the NiHCF/$MnO_2$ composites

The synthesis of all three NiHCF/$MnO_2$ composites is depicted in Fig. S1 (Supporting Information). Specifically, hierarchical core-shell structured NiHCF@λ-$MnO_2$ and NiHCF@δ-$MnO_2$ were prepared by depositing the $MnO_2$ particulates (shell) over the surfaces of the coprecipitated nickel hexacyanoferrate (NiHCF) cubes (core) hydrothermally or at room temperature (RT) (Fig. S1a), while α-$MnO_2$@-NiHCF was synthesized via embedding α-$MnO_2$ nanorods (core) over the NiHCF cubes (shell) at RT (Fig. S1b). The detailed preparation procedures of these NiHCF/$MnO_2$ composites can be found in Text S1. The crystallography, surface composition, surface functional groups, and morphology of the as-prepared NiHCF/$MnO_2$ materials were comprehensively studied. Specifically, X-ray diffraction (XRD) analysis was performed on an XRD-6100 diffractometer (XRD, Shimadzu, Japan) at a tube voltage of 40 kV and a tube current of 30 mA with Cu-Kα radiation. X-ray fluorescence spectroscopy (XRF) analysis was conducted on a DELTA DC 4000 analyzer (Olympus, USA) with the soil mode. Fourier transform infrared (FTIR) spectrum measurement was carried out following the KBr method on an infrared spectrometer (Nicolet iS5, Thermo Fisher, USA). The chemical states and surface composition of the as-synthesized NiHCF/MnO2 materials were further confirmed by X-ray photoelectron spectroscopy (XPS, UIVAC-PHI). The morphology of NiHCF/$MnO_2$ samples was examined on a ZEISS Gemini 300 field emission scanning electron microscope (SEM, ZEISS, Germany) and a Philips TECNAI 12 transmission electron microscope (TEM), respectively.

### 2.2. Electrochemical measurements

Cyclic voltammetry (CV), galvanostatic charge-discharge (GCD), and electrochemical impedance spectroscopy (EIS) analyses were performed in a 1.0 M lithium chloride (LiCl) solution using a three-electrode system on a CS310H electrochemical workstation (Correst Instruments Inc., Wuhan, China). The three-electrode configuration is composed of a working electrode, a platinum foil electrode (counter electrode), and an Ag/AgCl (3 M KCl) electrode (reference electrode). The working electrode was prepared by combining a specific composite (as the active materials), acetylene black (Alfa Aesar, Shanghai, China), and polyvinylidene fluoride (PVDF) in a mass ratio of 8:1:1. The mixture was ground by hand and dispersed in a slurry of 1-methyl-2-pyrrolidinone (NMP, Alfa Aesar), which then was deposited onto a graphite paper with a size of 1 × 1 $cm^2$ and dried in a vacuum at 80 °C. Approximately 1 mg of active material was loaded on each electrode. More details on electrochemical characterizations are presented in Text S2.

### 2.3. Capacitive deionization experiments

Following the same procedure for fabricating the working electrodes, the NiHCF/$MnO_2$ composite electrodes for CDI were fabricated in a size of 5 × 5 $cm^2$ (more details are given in Text S3). The desalination experiment was performed in a homemade rocking-chair capacitive deionization (RCDI) platform (Fig. S2) containing a custom-built CDI cell of a symmetric configuration of electrodes (Fig. S3). The RCDI cell was operated in batch mode and under constant voltage conditions for all the $Li^+$ extraction tests. Before the desalination test, the anode was prelithiated thrice in 3000 mg $L^{-1}$ of LiCl solution at 1.2 V for 40 min, embedding $Li^+$ ions into the anode structure (i.e., prelithiated anode) for the subsequent $Li^+$ extraction operation. A total of 40 mL of feed brine

was consecutively circulated between the RCDI cell (inside volume ~ 5 mL) and the feed brine reservoir at a flow rate of 40 mL $min^{-1}$. The conductivity of effluent was successively monitored by a DDSJ-308A conductivity meter (INESA Scientific Instrument Co., Shanghai, China) and used to calculate the $Li^+$ concentration. To examine the selectivity of NiHCF/$MnO_2$ electrodes, synthetic binary salt solutions of $Mg^{2+}/Li^+$ were prepared for the electrochemical lithium recovery experiments. In addition, East Taijinaier Salt Lake brine (Table S1, Supporting Information) was employed to assess the practicality of the electrode with the best CDI performance. The concentration of each ion before and after electrochemical lithium recovery was determined by an Optima 8300 (PerkinElmer, USA) inductively coupled plasma optical emission spectroscope (ICP-OES). More details about the $Li^+$ intercalation capacity, $Li^+$ selectivity coefficient, charge efficiency, and energy consumption are given in Text S3.

## 3. Results and discussion

### 3.1. Characterizations of the As-prepared NiHCF/$MnO_2$ composites

The hierarchical core-shell structured NiHCF/$MnO_2$ composites were prepared via wet-chemical synthetic routes (Fig. S1), with synthesis and characterization details given in the Experimental Section and supplementary Text S1. Depending on the synthetic conditions, the $MnO_2$ components in all NiHCF/$MnO_2$ composites varied from α-$MnO_2$ (with 2 × 2 tunnels of size 4.6 Å × 4.6 Å), λ-$MnO_2$ (with tunnel sizes of ~2.4–2.8 Å), to δ-$MnO_2$ (with an interlayer space of ~7 Å) [35], while NiHCF remains the cubic phase ($F\bar{4}3m$) with channels of theoretical size ~6.5 Å (Fig. 1b). X-ray diffraction showed that these reflections match up with the standard PDF cards of JCPDS #86-0501, #44-0141, #42-1169, and #80-1098, respectively (Fig. 1c), corresponding to cubic NiHCF, α-, λ-, and δ-$MnO_2$, respectively. Note that the reflections of λ- and δ-$MnO_2$ (marked with asterisks in the black and blue curves, Fig. 1c) are weak and somewhat broad, indicative of a poor crystallinity form of $MnO_2$ that can boost rapid diffusion of ions inside the active electrode materials by creating more diffusion pathways, shortening diffusion lengths, and reducing energy barriers [36] and thus enabling faster capacitive desalination [19]. Despite the diversity in the $MnO_2$ phase, X-ray fluorescence (XRF) revealed that all the composites demonstrate much the same elementary compositions, with Fe, Ni, and Mn being the three major detected elements (Fig. 1d). Note that the ratio of these major elements varied with composites, which is likely to ascribe to the difference in these core-shell microstructures, thus leaving varying proportions of NiHCF and $MnO_2$ exposed to air. Fourier transform infrared (FTIR) spectroscopy confirmed this observation as well (Fig. 1e), with typical IR bands assignable to hydroxyl groups (i.e., 3620, 3550, 3410, and 1620 $cm^{-1}$), $Fe^{III}$-CN-$Ni^{II}$ and $Fe^{II}$-CN-$Ni^{II}$ (2166 and 2100 $cm^{-1}$), and C≡N groups (1390 and 594 $cm^{-1}$) [31,37], respectively. Compared to α-$MnO_2$@NiHCF, NiHCF@λ-$MnO_2$ demonstrated the strongest IR band at 2100 $cm^{-1}$ (assignable to $Fe^{II}$-CN-$Ni^{II}$ groups), followed by NiHCF@δ-$MnO_2$, implying the order of NiHCF@λ-$MnO_2$ > NiHCF@δ-$MnO_2$ > α-$MnO_2$@NiHCF in terms of the exposure of NiHCF component within these composites. X-ray photoelectron spectroscopy (XPS) spectra further confirmed that the surface elemental compositions of the as-prepared NiHCF/$MnO_2$ composites (Fig. S4a) are consistent with the above spectroscopic results (Fig. 1c–e). Notably, XPS spectra of the Fe 2p, Ni 2p, and Mn 2p regions (Fig. 1f–h) indicated that their oxidation states are +3, +2, and +4, respectively [31,38,39], aligning with the above XRD and FTIR data.

Field emission scanning electron microscopy (SEM) revealed that both the NiHCF@λ-$MnO_2$ and NiHCF@δ-$MnO_2$ had a hierarchical core-shell feature, seemingly with cubic NiHCF (highlighted with blue squares) as the cores and nanoaggregate-like λ-$MnO_2$ and flower-like δ-$MnO_2$ as the shells, respectively (Fig. 2b, c). Both core-shell composites exhibited an irregular spherical porous surface topography, offering a larger specific surface area and a shorter ion diffusion path, favorable

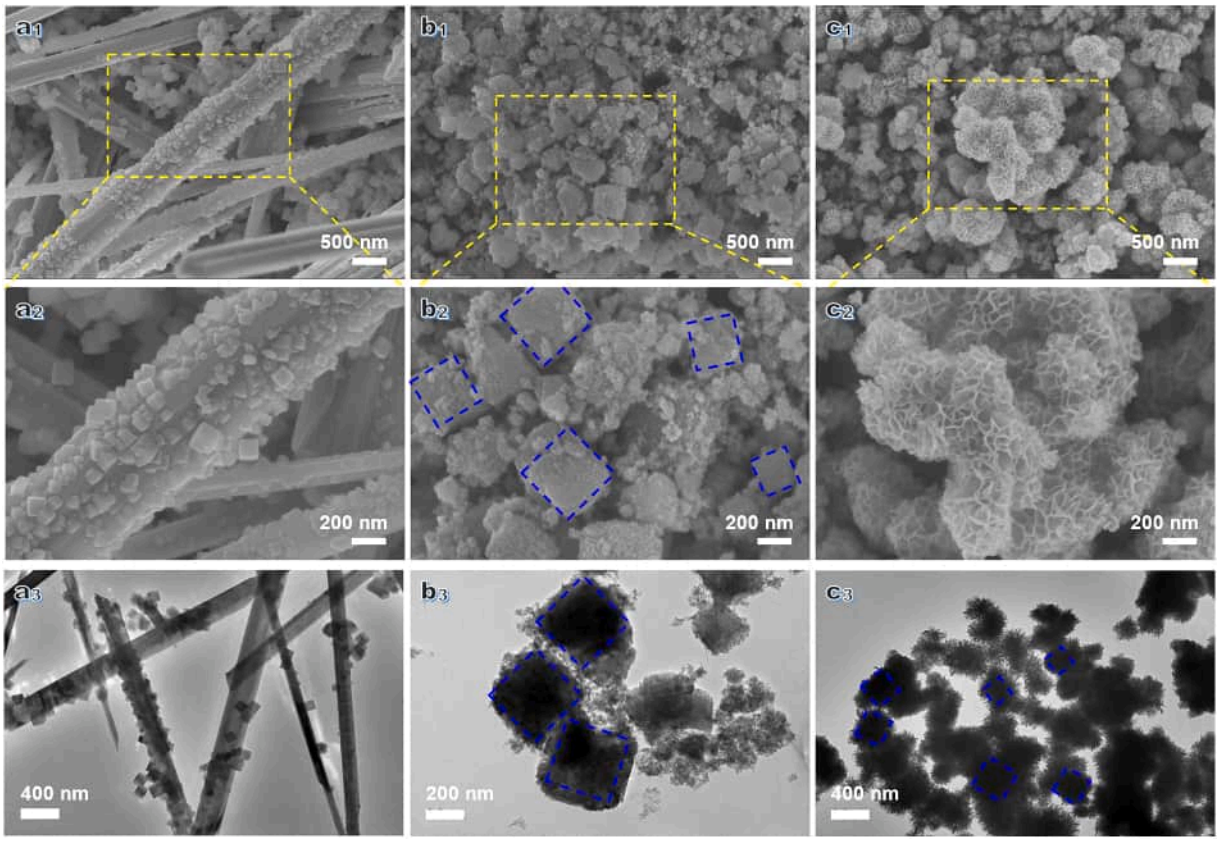


**Fig. 2.** SEM and TEM images of the as-prepared (a) α-$MnO_2$@NiHCF, (b) NiHCF@λ-$MnO_2$, and (**c**) NiHCF@δ-$MnO_2$.

to ion transport and insertion/extraction, with improved ion uptake [40]. In contrast, α-$MnO_2$@NiHCF was prepared with α-$MnO_2$ as the core and NiHCF as the shell, where the α-$MnO_2$ had a needle-like morphology with numerous well-defined cubic NiHCF particles uniformly embedded over their surface (Fig. 2a). Transmission electron microscope (TEM) confirmed the above morphological features of these composites (Fig. 2$a_3$–$c_3$).

### 3.2. Electrochemical properties of the NiHCF/$MnO_2$ electrodes

To explore the correlation between the microstructure features and the potential capacitive $Li^+$ extraction properties of NiHCF/$MnO_2$ composites, we evaluated their electrochemical performance in a 1.0 M LiCl solution using a three-electrode system (Text S2). Unlike conventional carbon-based electrodes, both NiHCF and $MnO_2$ are Faradaic (charge-transfer) materials [33], whose cyclic voltammetry (CV) curves are often featured by a pair of identifiable redox peaks (Fig. S5a) corresponding to Faradaic reactions of $Fe^{III}(CN)_6 + e^- \rightleftharpoons Fe^{II}(CN)_6$ and $Mn^{IV}O_2 + e^- \rightleftharpoons Mn^{III}O_2$, respectively [29,30,37,39]. Upon assembly by wet-chemical routes into NiHCF/$MnO_2$ composites, these redox peaks are still retained, with shifts in their positions and peak shapes due to differences in interfacial ion transport behavior derived from the unique microstructures of these composites (Fig. 3a). Note that the CV curve areas of the three composites follow the order of NiHCF@λ-$MnO_2$ > NiHCF@δ-$MnO_2$ > α-$MnO_2$@NiHCF, indicating the same trend in their charge storage capacity [41]. To quantitatively differentiate between the diffusion- and capacitive-controlled charge storage process of these composites, we collected the CV curves at multiple scan rates (5–10 mV $s^{-1}$, Fig. S5b–d) and explored the relationship between log*i* and log*v* using the *b*-value analysis based on the redox peak $O_{X2}$ with a lower peak current (Fig. S5) [42]. Compared to α-$MnO_2$@NiHCF and NiHCF@δ-$MnO_2$ with *b*-values of 0.719 and 0.769, respectively (Fig. 3b), NiHCF@λ-$MnO_2$ showed the greatest *b*-value of 0.824, implying its capacitive-dominant charge-storage behavior in nature [43]. Calculation based on Dunn's algorithm showed that the contributions from capacitive-controlled (pseudocapacitive) charge-storage increased with the scanning rate (Fig. S6) [43], since $Li^+$ ions are likely to be involved in the pseudocapacitive behavior (surface-Faradaic reaction) rather than the diffusive-controlled intercalation process (Faradaic reaction), particularly at a higher scanning rate [19]. Note that the calculated $Li^+$ diffusion coefficient of NiHCF@λ-$MnO_2$ was much higher than those of α-$MnO_2$@NiHCF and NiHCF@δ-$MnO_2$, respectively (Fig. S7 and Table S2), demonstrating the effective enhancement of $Li^+$ diffusion transfer through the core-shell construction strategies. For instance, the contributions from pseudocapacitive charge-storage varied from 54.2 %, 40.6 % to 35.9 % for NiHCF@λ-$MnO_2$, NiHCF@δ-$MnO_2$, and α-$MnO_2$@NiHCF, respectively, at a scan rate of 10 mV $s^{-1}$ (Fig. 3c), indicating that the core-shell structured NiHCF@λ-$MnO_2$ has a hierarchical interface favorable for pseudocapacitive charge-storage. This is consistent with the results of *b*-value analysis (Fig. 3b), and also confirms the above morphological observations (Fig. 2b), with the shell-layered λ-$MnO_2$ contributing majorly to the pseudocapacitive charge-storage process [44].

Galvanostatic charge-discharge (GCD) analysis revealed that all the NiHCF/$MnO_2$ electrodes demonstrate symmetric triangular charge-discharge profiles with slight deviations in linearity and minor iR (ohmic) drops in the discharge branches (Figs. 3d, S8), indicative of high reversibility and low internal resistance of the electrochemical system (Table S3). The minor linearity deviations are derived from the Faradaic and pseudocapacitive behaviors of these composite electrodes [39].

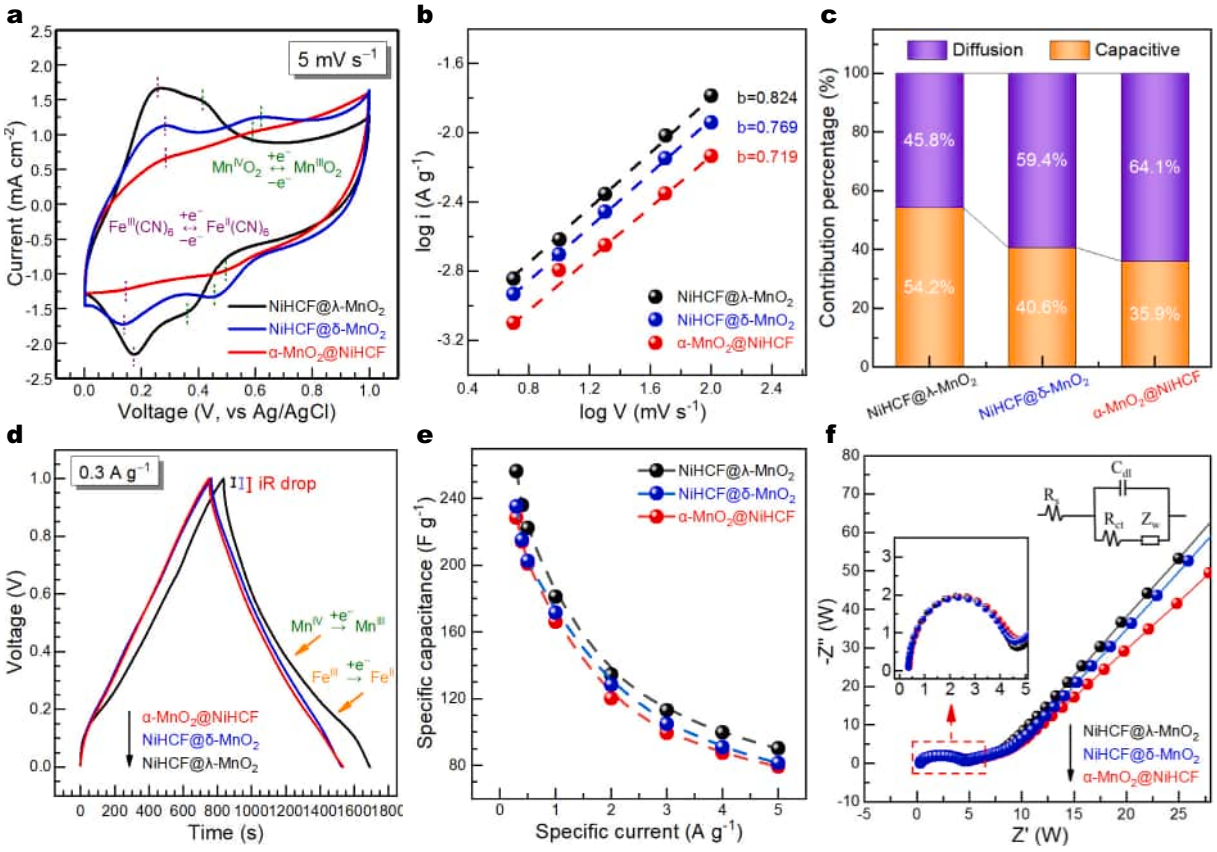


**Fig. 3.** Electrochemical characterizations of NiHCF/$MnO_2$ electrodes: (a) CV curves at 5 mV $s^{-1}$ in 1 M LiCl solution; (b) calculated *b*-values of redox peaks based on the CV curves of all electrodes at varying scan rates (5–100 mV $s^{-1}$); (c) contribution percentage of diffusion- and capacitive-controlled capacitance at a scan rate of 10 mV $s^{-1}$; (d) GCD curves at 0.3 A $g^{-1}$ in 1 M LiCl solution; (e) specific capacitances at different specific currents; (f) Nyquist plots of EIS and the fitting curves, the top-right inset is the equivalent circuit.

Note that the NiHCF@λ-$MnO_2$ electrode exhibited a longer discharge plateau (highlighted with two orange arrows in Fig. 3d, which correlated to the reduction of $Mn^{IV}$ and $Fe^{III}$ reactions, respectively) relative to the other electrodes, indicating a higher specific capacitance of the NiHCF@λ-$MnO_2$ electrode [45]. These results are in agreement with the above speculation based on the CV curve (Fig. 3a). Additionally, the NiHCF@λ-$MnO_2$ electrode also showed the smallest iR drop among all the NiHCF/$MnO_2$ electrodes (Table S3), indicative of the lowest internal charge transfer resistance and excellent capacitive performance [38]. Specific capacitances were determined from GCD curves in line with the standard method [46], and are found to decrease with the specific current due to the limitations of charge transfer and ion transport (Fig. 3e) [47]. For instance, the specific capacitances ($C_s$) are 256.35, 235.24, and 228.51 F $g^{-1}$ at a specific current of 0.3 A $g^{-1}$ for NiHCF@λ-$MnO_2$, NiHCF@δ-$MnO_2$, and α-$MnO_2$@NiHCF, respectively (Table S3), with the NiHCF@λ-$MnO_2$ electrode demonstrating the highest specific capacitance and probably the largest $Li^+$ ion storage capacity. Moreover, we further evaluated the charge transfer resistance and ion diffusion properties of these electrodes using electrochemical impedance spectroscopy (EIS) and found that the charge transfer resistances ($R_{ct}$), determined by the diameters of the quasi-semicircles in the high-frequency region (Fig. 3f), were 3.60, 3.62 and 3.79 Ω for NiHCF@λ-$MnO_2$, NiHCF@δ-$MnO_2$, and α-$MnO_2$@NiHCF, respectively (Table S3). Note that the α-$MnO_2$@NiHCF electrode has the largest $R_{ct}$ and the smallest straight-line slope compared to NiHCF@λ-$MnO_2$ and NiHCF@δ-$MnO_2$ (Fig. 3f). This is likely attributed to α-$MnO_2$@NiHCF with the well-defined and compact NiHCF nanocrystals as the shell layers (Fig. 2a), which results in slow diffusion of ions across the electrode/electrolyte interface [19]. The best-fit results in Table S3 show that the NiHCF@λ-$MnO_2$ electrode displayed the greatest electrical conductivity in terms of its lowest equivalent series resistance ($R_s$), underscoring its best electrochemical properties. Collectively, we can envision that the NiHCF@λ-$MnO_2$ electrode with the highest ion storage capacity ($C_s$) and the lowest $R_{ct}$ and $R_s$ should be the best electrode candidate for capturing $Li^+$ ions.

### 3.3. $Li^+$ Extraction performance

To compare and single out the optimal $Li^+$ extraction electrode for different scenarios, we comprehensively evaluated the $Li^+$ extraction performance of all the NiHCF/$MnO_2$ electrodes at different voltages (0.6, 0.8, 1.0 and 1.2 V) and varying concentrations (5, 10 and 20 mM) for three different metrics: salt adsorption capacity ($\Gamma$), salt adsorption rate (*SAR*) and energy consumption (Text S3). All the electrochemical $Li^+$ extraction tests were performed in batch mode on a homemade RCDI module (Fig. S2) with a well-assembled cell configuration (Fig. S3). Fig. 4a shows the conductivity plots of the cell solution (0.5 mM LiCl) during one charge-discharge run at 1.2 V, whereas Fig. 4b depicts the corresponding $\Gamma$ values and $Li^+$ adsorption percentage ($Li^+$ adsorption %). Generally, the conductivity curves feature an electrosorption phase, a saturation phase, and a desorption phase [29]. Note that both the α-$MnO_2$@NiHCF and the NiHCF@δ-$MnO_2$ electrodes achieved a saturation state in the 40-min charging stage (the yellow-shaded region, Fig. 4a). In contrast, the NiHCF@λ-$MnO_2$ electrode was far from an

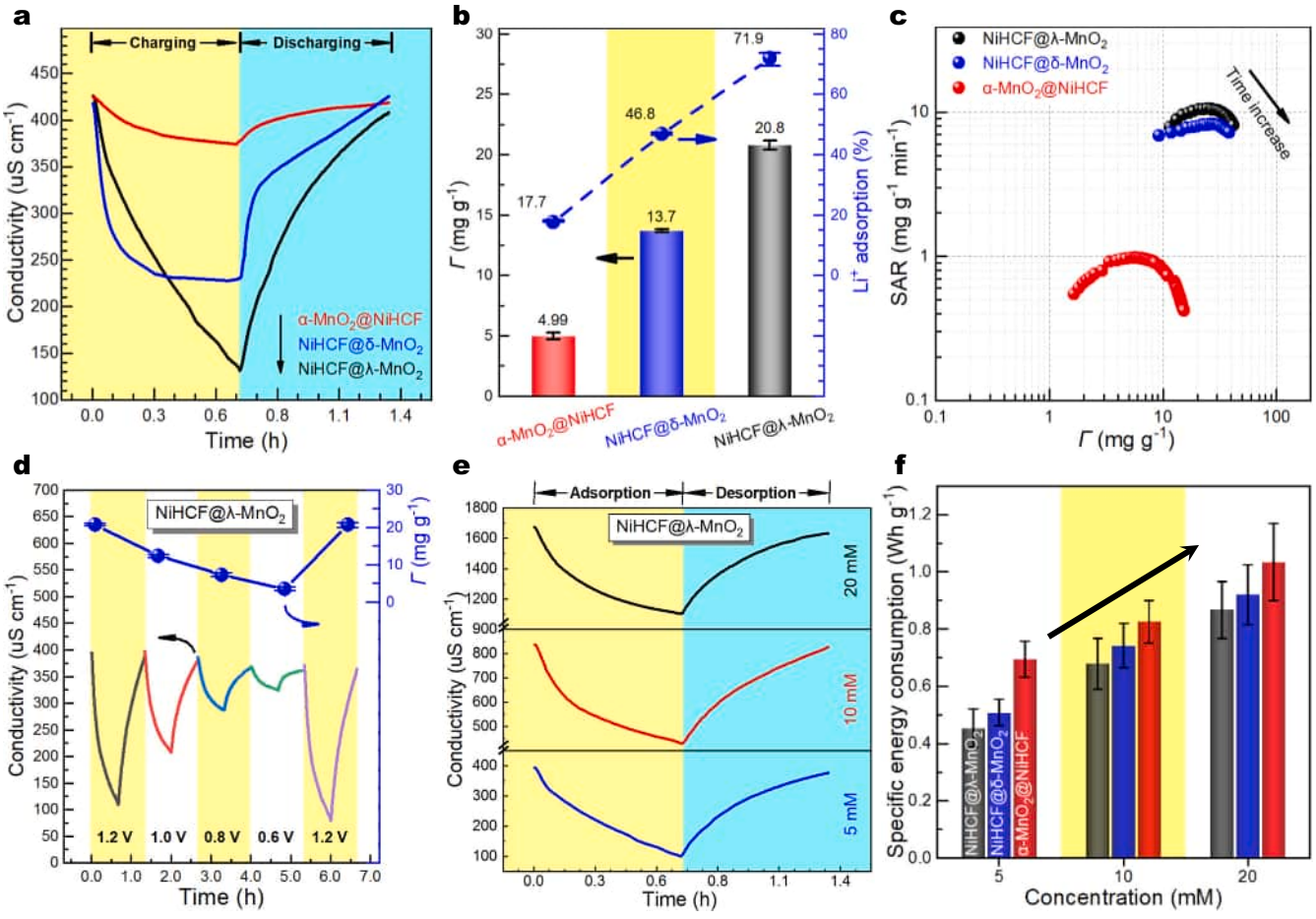


**Fig. 4.** (a) Plots of conductivity versus time in one charge-discharge operation of CDI with NiHCF/$MnO_2$ electrodes in 5 mM $Li^+$ ion solution at 1.2 V; (b) $Li^+$ adsorption capacity and efficiency of three NiHCF/MnO2 composite electrodes in 5 mM LiCl solution; (c) Kim-Yoon plots; (d–e) plots of conductivity versus time of the CDI cell with NiHCF@λ-$MnO_2$ electrodes at (d) different voltages in 5 mM LiCl solution and (e) with varying concentrations at 1.2 V; (f) energy consumption of NiHCF/$MnO_2$ electrodes versus feedwater salt concentration at 1.2 V.

equilibrium after charging for 40 min, indicating its higher capacity for capturing $Li^+$ relative to the other NiHCF/$MnO_2$ electrodes. For the sake of consistency, the subsequent $Li^+$ extraction experiments were performed following the same protocol (i.e., charging for 40 min followed by discharging for 40 min) [37]. The $Li^+$ adsorption capacities ($\Gamma$) were 4.99, 13.7 and 20.79 mg $g^{-1}$ for α-$MnO_2$@NiHCF, NiHF@δ-$MnO_2$ and NiHF@λ-$MnO_2$ electrodes, respectively (Fig. 4b), with the corresponding $Li^+$ adsorption% varying from 17.7 %, 46.8 % to 71.9 %, in good consistence with the ion storage capacity deduced above (Fig. 3e). Interestingly, the α-$MnO_2$@NiHCF electrode showed a relatively poor capacity for $Li^+$, accounting only for 36.4 % and 24.0 % of those of NiHF@δ-$MnO_2$ and NiHF@λ-$MnO_2$ electrodes, respectively. This lower adsorption capacity of α-$MnO_2$@NiHCF is possibly attributed to the lower ion-transport rate and selectivity of the highly crystalline NiHCF layers (see Fig. 2a) for $Li^+$ than the shell-layered $MnO_2$, and to the mismatched interfacial kinetics of $Li^+$ diffusion, thereby depressing $Li^+$ ions from entering the lattice of the α-$MnO_2$ core [12,48]. However, both NiHCF@δ-$MnO_2$ and NiHCF@λ-$MnO_2$ composites with $MnO_2$-based shell layers exhibited higher $Li^+$ extraction performance, indicating that the $\Gamma$ is highly dependent on both the composition of the shell layers and the interfacial configuration of the core-shell layers, and that $MnO_2$-based shell layers demonstrated a higher affinity for $Li^+$ than the crystalline NiHCF layers. Additionally, further analysis based on the Kim-Yoon plotting indicated that the distance between the *SAR* vs $\Gamma$ contour lines and the upper right corner of the coordinate frame increased in the order of NiHCF@λ-$MnO_2$ < NiHCF@δ-$MnO_2$ < α-$MnO_2$@NiHCF (Fig. 4c), suggesting that NiHCF@λ-$MnO_2$ electrode can capture much more $Li^+$ ions at the highly fastest rate (e.g., obtaining the highest $\Gamma$ of 43.51 mg $g^{-1}$ at a SAR of 8.1 mg $g^{-1}$ $min^{-1}$, Fig. 4c) [30]. Fig. S9 depicts the current response, charge efficiency and the Faradaic efficiency of these electrodes in 5 mM of LiCl solution at 1.2 V. Notably, the NiHCF@λ-$MnO_2$ electrode exhibited the highest current level, the greatest charge efficiency (0.87 vs 0.81, 0.71 for NiHCF@δ-$MnO_2$ and α-$MnO_2$@NiHCF, respectively) and the largest Faradaic efficiency (0.97 vs 0.84, 0.75 for NiHCF@δ-$MnO_2$ and α-$MnO_2$@NiHCF, respectively), further confirming the superiority of NiHCF@λ-$MnO_2$ electrode relative to its other counterparts in highly efficient $Li^+$ extraction from brines.

Like most other Faradaic materials in CDI toward desalination [29,31,33], the $Li^+$ extraction capacities of these NiHCF/$MnO_2$ electrodes are vastly dependent on both the cell voltage and the feed saline concentration (Figs. 4d–e, S10, S11). A higher voltage (e.g., 1.2 V) can generate a much larger insertion driving force for these NiHCF/$MnO_2$ electrodes to capture $Li^+$ ions via either Faradaic or pseudocapacitive processes (Fig. 3a), and thereby yielding a higher $Li^+$ adsorption capacity [49]. Note that the corresponding $\Gamma$ decreased with the cell voltage from 1.2 to 0.6 V linearly and recovered to the initial values instantly when the cell voltage reclaimed to 1.2 V (Figs. 4d and S10), verifying that all these NiHCF/$MnO_2$ electrodes have a very sensitive response to different voltages and showcasing their potential for lithium extraction. Apart from the driving force from cell voltage (i.e., electrochemical gradient), feed saline with a higher salt concentration is expected to yield another driving force from the concentration difference between the bulk electrolyte and the electrode surface (i.e., concentration gradient) [50], with a shorter period to reach the equilibrium state (Fig. 4e) and achieving a higher $\Gamma$ at a higher salt concentration for all these NiHCF/$MnO_2$ electrodes (Fig. S12). For instance, the NiHCF@λ-$MnO_2$ electrode showed a maximum $\Gamma$ of 43.51 mg $g^{-1}$ in a feed saline with 20 mM of $Li^+$ ions, outranking the other two NiHCF/$MnO_2$ electrodes (Fig. S12) as well as other $MnO_2$-based electrodes reported in the literature for $Li^+$ extraction (Table S4). Considering the theoretical limits for both pure NiHCF (~40–48 mg $g^{-1}$ for a two-electron transfer, or ~ 20–24 mg $g^{-1}$ for a one-electron transfer) and λ-$MnO_2$ (~38–40 mg $g^{-1}$) [48,51], the composite NiHCF@λ-$MnO_2$ exhibits a synergistic effect that enhances its $Li^+$ adsorption capacity beyond what would be expected from the simple sum of its individual components. The interfacial synergy between NiHCF and λ-$MnO_2$ (i.e., the interlayer concentration enhancement (ICE) effect) [52] boosts the electron transfer and ion mobility in the hierarchical core-shell NiHCF@λ-$MnO_2$ electrode, where the NiHCF core appears to serve as the main $Li^+$ reservoir due to its high theoretical capacity, while the λ-$MnO_2$ shell is likely to act as the $Li^+$ ion-sieve owing to its narrow ion channels favorable to $Li^+$ over $Na^+$/$K^+$ and other divalent cations. In addition, the uniform coating of λ-$MnO_2$ on the NiHCF core may create an interfacial electric field for more ions to accumulate in the porous channels, which finally enhances the $Li^+$ extraction performance. Nevertheless, the enhanced $Li^+$ extraction capacity aligns with interfacial synergy effects observed in analogous core-shell systems [52,53], though direct mechanistic validation requires further study (DFT and operando spectroscopy).

Energy consumption is another important factor in determining CDI performance. Normalized energy consumption for all NiHCF/$MnO_2$ electrodes during $Li^+$ extraction operations exhibited a direct positive correlation with salt concentration (Fig. 4f; Text S3). This relationship is attributed to the increased solution resistance and enhanced electrode polarization observed at higher ionic strengths, which consequently elevates the specific energy consumption [54]. Notably, the NiHCF@λ-$MnO_2$ electrode demonstrated the highest energy efficiency among these NiHCF/$MnO_2$ electrodes. For instance, only 0.45 Wh per gram $Li^+$ was consumed for the extraction of $Li^+$ in a 5 mM LiCl solution by the RCDI system with NiHCF@λ-$MnO_2$ electrodes. Collectively, the NiHCF@λ-$MnO_2$ electrode exhibits a superior lithium extraction performance concerning the above metrics (i.e., $\Gamma$, *SAR*, and normalized energy consumption), and ranks the top among the reported $MnO_2$-based electrodes for $Li^+$ extraction (Table S4), demonstrating its bright promise to extract $Li^+$ ions from brines. In light of this unique superiority, we chose the NiHCF@λ-$MnO_2$ electrode as the sole candidate for further exploring its cycling and selectivity properties.

### 3.4. Cycling performance of the NiHCF@λ-$MnO_2$ electrode

Generally, CDI electrodes often suffer from structural degradation and performance deterioration upon consecutive charge/discharge within the CDI cells [55]. We then further explored the cycling performance of the NiHCF@λ-$MnO_2$ electrode in 10 mM LiCl solution and at a voltage of 1.2 V, given its superior electrochemical and lithium extraction performance relative to other NiHCF/$MnO_2$ electrodes. Remarkably, the NiHCF@λ-$MnO_2$ electrode showed an initial $\Gamma$ as high as 39.99 mg $g^{-1}$, which was stable in the first 10 cycles, and then declined to 37.69 mg $g^{-1}$ at the end of the 10th run, with a capacity retention of 94.2 % (Fig. 5a, b). As the cycle number increased, the $Li^+$ extraction capacity decreased linearly to a final $\Gamma$ of 31.37 mg $g^{-1}$, with a capacity retention of 78.4 % after 40 cycles of continuous adsorption-desorption operations, showcasing a typical performance deterioration profile of $MnO_2$-based electrodes applied to CDI with a relatively good cyclability [30,41]. Interestingly, the solution pH values recorded every four cycles appear to fluctuate with a well-defined rhythm between 8.3 and 11, with a consequent decrease in pH when adsorption started and an increasing pH during the desorption stages. This phenomenon is likely attributed to the Faradaic reactions (i.e., $MnO_2 + Li^+ + e^- \rightleftharpoons LiMnO_2$ and $Fe^{III}(CN)_6 + Li^+ + e^- \rightleftharpoons LiFe^{II}(CN)_6$, Text S3) during the charging/discharging operations, leading to local generation or consumption of protons and thus the observed pH fluctuations [56,57].

Given the fact that both the NiHCF and the $MnO_2$ crystals are prone to dissolve in solutions with an alkaline pH (>8) and upon repeated cycling [41,58], the cycle-dependent $Li^+$ extraction performance deterioration may arise from: i) $Ni^{2+}$/$Fe^{3+}$ leaching from the NiHCF lattice [31], ii) the Jahn-Teller distortion in $MnO_2$ during $Li^+$ insertion/extraction and thus partial dissolution of $MnO_2$ [20,41], and iii) potential interfacial delamination in the core-shell structure [59]. To further explore the underlying mechanisms and evaluate the structural stability of the NiHCF@λ-$MnO_2$ electrode after 40 cycles, XRD, XRF, and FTIR data of the post-cycling electrode were collected and compared to the pristine NiHCF@λ-$MnO_2$ (Fig. 5c–e). Comparison of the XRD patterns

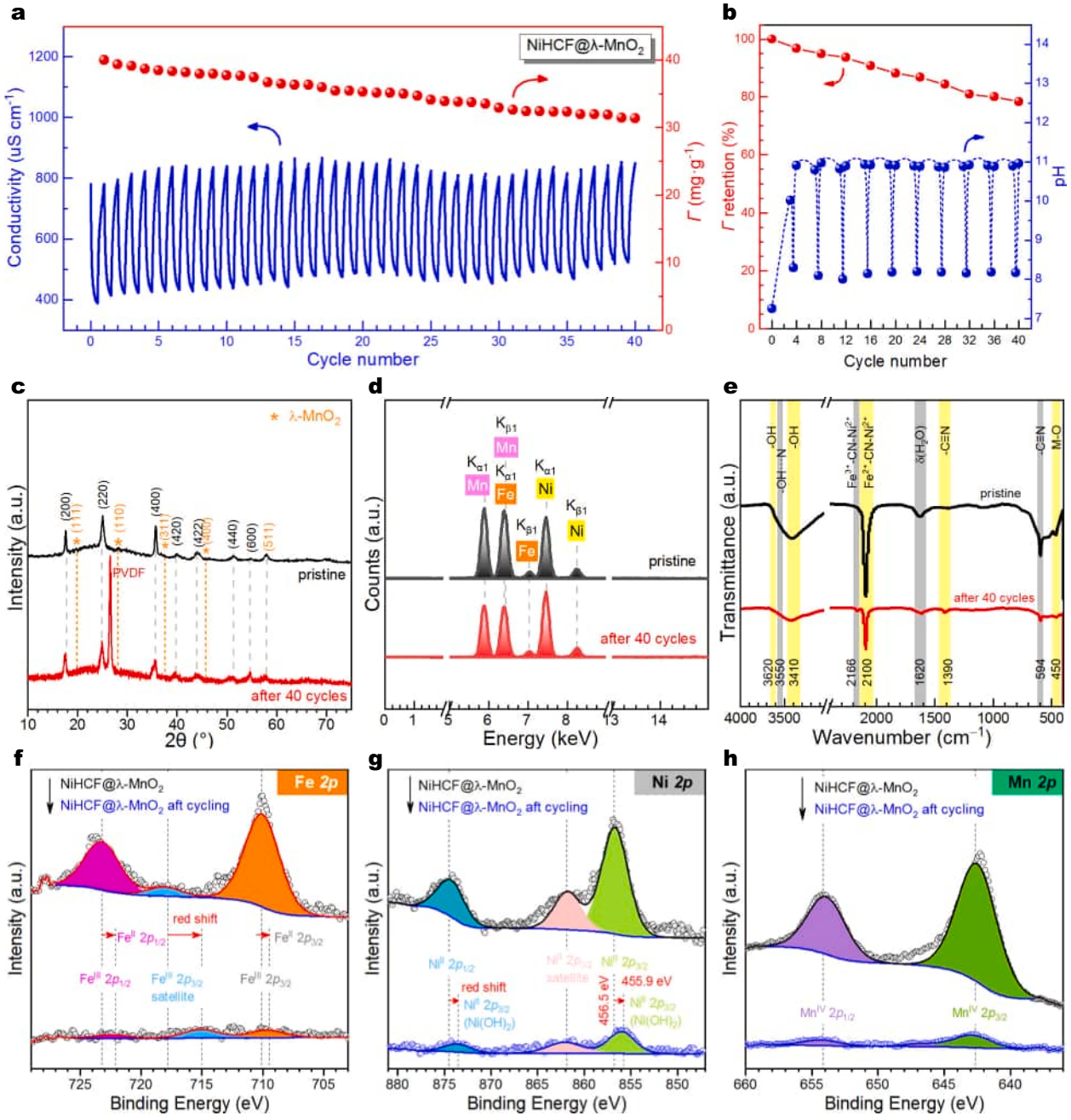


**Fig. 5.** (a) Cycling stability and adsorption capacity, (b) the corresponding changes in capacity retention and pH of NiHCF@λ-$MnO_2$ electrode in 10 mM LiCl solution applied in RCDI for 40 charge-discharge runs; (c) XRD patterns, (d) XRF, (e) FTIR, and (f-h) XPS spectra of the Fe 2p (f), Ni 2p (g) and Mn 2p (h) regions of the as-prepared NiHCF@λ-$MnO_2$ composite and the post-cycling NiHCF@λ-$MnO_2$ electrodes.

indicates that both the NiHCF and the λ-$MnO_2$ appear to fade over cycling in alkaline environment (Fig. 5c). Notably, there is a well-defined diffraction peak attributable to PVDF in the pattern of the post-cycling electrode, which is derived from the PVDF binder added in the preparation of the electrode, but not in the as-prepared (pristine) NiHCF@λ-$MnO_2$ (Fig. 5c). After cycling for 40 runs, both the XRF and FTIR results confirmed that the shell-layered λ-$MnO_2$ seems to lose partially as evidenced indirectly by the slight decline of the principal $K_{\alpha 1}$ shell of element Mn (5.9 keV, Fig. 5d) and the weakening of the IR band of M-O (~ 450 $cm^{-1}$, Fig. 5e). On the one hand, repeated $Li^+$ intercalation/deintercalation can induce lattice strain in λ-$MnO_2$, accelerating structural degradation [60]. On the other hand, hydroxyl ions ($OH^-$) may promote partial Mn leaching since it's amphoteric and becomes increasingly unstable in strong alkali (pH > 10–12) [61]. XPS analysis also verified the structural degradation of both the NiHCF and the λ-$MnO_2$ components over cycling (Fig. 5f–h). Note that both the Fe 2p and the Ni 2p peaks shifted toward a lower energy direction ('red shift') after cycling, while Mn 2p remained. A possible explanation is that λ-$MnO_2$ served as the shell layer without a diffusion barrier for the lithiation-delithiation reactions, thus kinetically facilitating the transformation of $Mn^{IV}$ from $Mn^{III}$ (i.e., delithiation via $LiMn^{III}O_2 \rightarrow Mn^{IV}O_2 + Li^+ + e^-$). However, delithiation reactions in the core NiHCF components were kinetically limited by the diffusion barriers (i.e., λ-$MnO_2$ shells), rendering the Fe of NiHCF into an oxidation state of +2 (i.e., $LiFe^{II}(CN)$, Fig. 5f). Regarding Ni 2p, the 'red shift' is likely due to the formation of $Ni(OH)_2$ with lower binding energy of Ni 2p during the cycling in brines, confirm the dissolution of nickel element along with iron from NiHCF components as observed above.

Nevertheless, the absence of any characteristic peaks of oxygen evolution reaction (OER) or hydrogen evolution reaction (HER) in the CV curves (Fig. 3a) further excludes the occurrence of such side reactions during the cycling operations. To mitigate this performance deterioration, the primary strategy is to operate the CDI-based $Li^+$ extraction within a narrow, optimized pH window (e.g., ~ neutral pH). Besides, prospective strategies such as coating with protective conductive films and/or doping with other elements have been demonstrated to effectively enhance durability beyond pH control [31,62]. Collectively, the above results suggest that the NiHCF@λ-$MnO_2$ electrode exhibits moderate cycling performance over 40 cycles of $Li^+$ extraction operation and that structural degradation of the shell-layered λ-$MnO_2$ contributed primarily to the capacity fade of the electrode during cycling. Nevertheless, the data from these short-term cycling tests in our lab-scale study are far from sufficient for scaling up our RCDI system for practical applications. Future works are necessary to address the scalability of our current systems based on strategies including module design and stacking, flow field engineering, system integration, etc., for advancing it toward practical use [63].

### 3.5. Selectivity of the NiHCF@λ-$MnO_2$ electrode for $Li^+$ ions

The selectivity of NiHCF@$MnO_2$ for $Li^+$ was initially performed in a synthetic brine containing 10 mM of cations found in the diluted brine from the East Taijinaier Salt Lake (i.e., $Li^+$, $Na^+$, $Ca^{2+}$, $Mg^{2+}$, and $Pb^{2+}$, see Table S1), and was measured by a separation factor, β, defined as the ratio of $Li^+$% captured to that of another cation by the electrodes via RCDI (Text S3). Driven by the potential difference between the cathode and the anode, the concentrations (***C***) of all cations were found to decrease over time expectedly (Fig. S13), leading to approximately linear increases in cation concentration variation (Δ***C***, defined as the concentration difference between two consecutive samples) over time in the synthetic brine (Fig. 6a). These Δ***C*** demonstrated a clear slope in the order of $Li^+ \gg Na^+ > Ca^{2+} > Mg^{2+} > Pb^{2+}$, indicative of the highest preference of the NiHCF@λ-$MnO_2$ electrode toward $Li^+$ over other cations separately due to the profound affinity of spinel λ-$MnO_2$ for $Li^+$ ions [64]. Note that $Li^+$ concentration plummeted faster than ever and other cations from 5 to 10 min (Fig. S13a), implying a faster $Li^+$ extraction kinetic in this short period, which is identical to the initial slump in

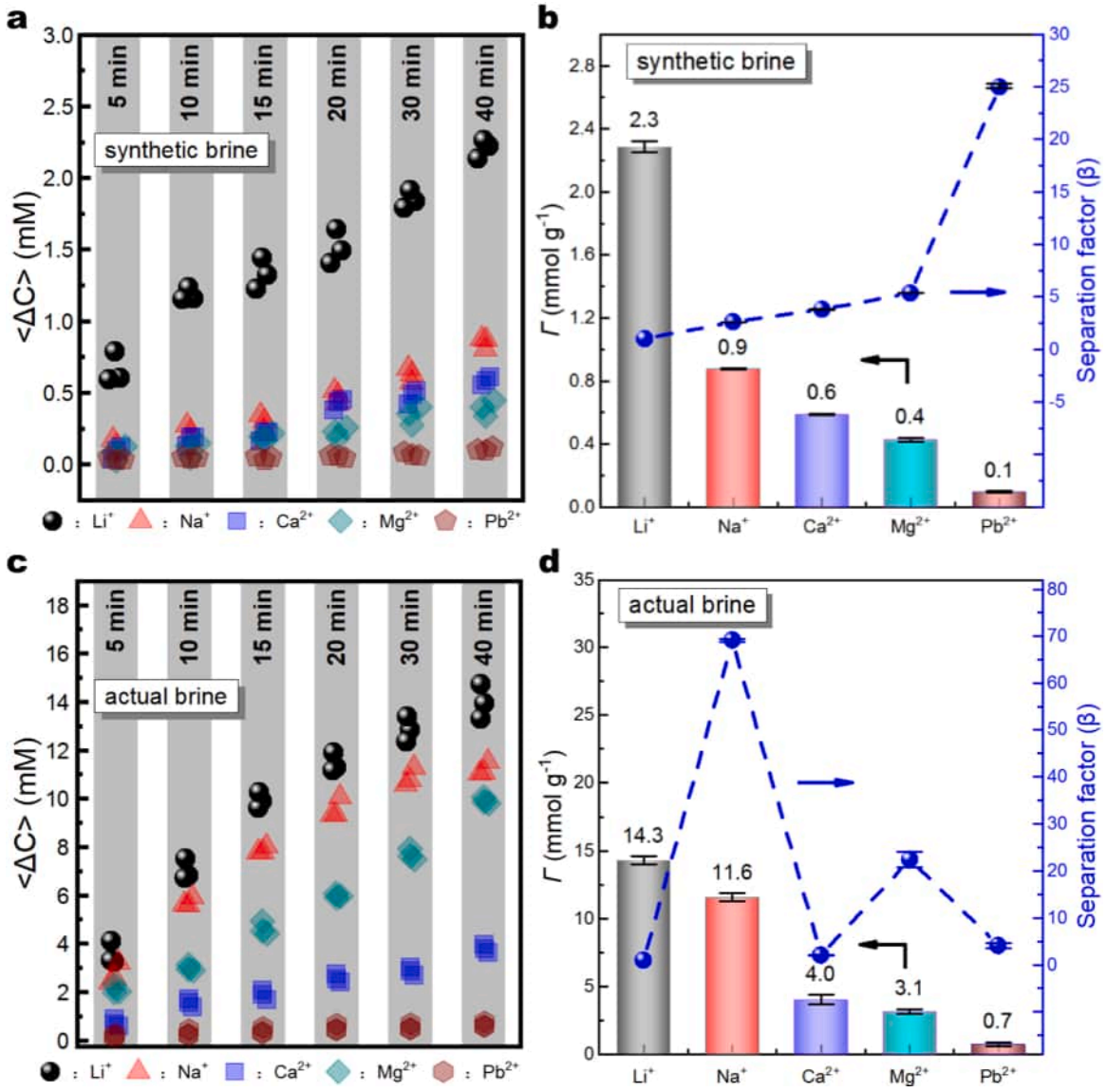


**Fig. 6.** (a) Cation concentration variation (Δ***C***) over time in the synthetic brine (10 mM of $Li^+$, $Na^+$, $Ca^{2+}$, $Mg^{2+}$, $Pb^{2+}$), (b) the corresponding cation capacity (***Γ***, mmol $g^{-1}$) and separation factor (***β***) for $Li^+$, (**c**) cation concentration variation (Δ***C***) over time in the brine of the East Taijinaier Salt Lake (59.4 mM $Li^+$, 3289.8 mM $Na^+$, 32 mM $Ca^{2+}$, 269.1 mM $Mg^{2+}$, and 8.9 mM $Pb^{2+}$), (d) the corresponding ***Γ*** and separation factor (note: the blue dash lines in panels b, and d are used only for visual guidance).

conductivity observed earlier (Fig. 4a). This phenomenon confirms the preference of NiHCF@λ-$MnO_2$ electrode for $Li^+$ ions. As shown in Fig. 6b, the adsorption capacities ($\Gamma$, in mmol $g^{-1}$) of the NiHCF@λ-$MnO_2$ electrode for these cations varied in the same order as the above $\Delta C$ slops (Fig. 6a), i.e., $\Gamma_{Li}$ (2.3 mmol $g^{-1}$, i.e., 15.96 mg $Li^+$ $g^{-1}$) > > $\Gamma_{Na}$ (0.9 mmol $g^{-1}$) > $\Gamma_{Ca}$ (0.6 mmol $g^{-1}$) > $\Gamma_{Mg}$ (0.4 mmol $g^{-1}$) > $\Gamma_{Pb}$ (0.1 mmol $g^{-1}$), with the relevant separation factor ($\beta_{Li/M}$) following to a reverse order of $\beta_{Li/Pb}$ (25.0) > > $\beta_{Li/Mg}$ (5.4) > $\beta_{Li/Ca}$ (3.8) > $\beta_{Li/Na}$ (2.6). This data verified the higher preference of the NiHCF@λ-$MnO_2$ electrode for $Li^+$ ions over other cations, in good agreement with previous reports for individual NiHCF and λ-$MnO_2$ electrodes [20,37].

To explore its practical applicability in a real brine, the NiHCF@λ-$MnO_2$ electrode was then tested in an actual brine collected from the East Taijinaier Salt Lake (Qinghai, China) with $Li^+$ ions as high as 59.4 mM (Table S1). Unlike the synthetic brine with an identical ionic concentration of 10 mM, the chemical composition of the East Taijinaier Salt Lake brine varied significantly, with remarkable $Na^+/Li^+$ and $Mg^{2+}/Li^+$ molar ratios as high as 55.38 and 4.53, respectively (Table S1), which are expected to impact its selectivity greatly [65]. Similar trends of $\Delta C$ and $\Gamma$ were observed in the tests of $Li^+$ extraction from the real brine regardless of its composition (i.e., 59.4 mM of $Li^+$, 3289.8 mM of $Na^+$, 32 mM of $Ca^{2+}$, 269.1 mM of $Mg^{2+}$, and 8.9 mM of $Pb^{2+}$) (Fig. 6c, d), demonstrating the excellent $Li^+$ selectivity of the NiHCF@λ-$MnO_2$ electrode was preserved in a real brine. For instance, as time increased from 0 to 40 min, the $Li^+$ concentration decreased linearly from 59.4 to 45.5 mM (Fig. S13b), with a maximum $\Delta C$ of 13.9 mM (Fig. 6c) and a corresponding $\Gamma_{Li}$ of 14.3 mmol $g^{-1}$ (99.24 mg $Li^+$ $g^{-1}$) (Fig. 6d), demonstrating the highest electrochemical $Li^+$ extraction capacity from the East Taijinaier Salt Lake brine reported so far [31]. It is noteworthy that, in the actual brine with higher M/Li (M = Na or Mg) molar ratios (i.e., $Na^+/Li^+$ = 55.38, $Mg^{2+}/Li^+$ = 4.53), $\Gamma_{Na}$ and $\Gamma_{Mg}$ have been increased by 12.9 and 7.8 times, respectively, confirming the salt concentration dependence of the ion adsorption capacity as observed above (Fig. 4e,f). Recall the fact that an increase in the ionic concentration can increase the concentration gradient, thereby driving more $Na^+$ and/or $Mg^{2+}$ ions to transfer and intercalate into the electrodes along with $Li^+$ ions. As a consequence, the corresponding separation factors, $\beta_{Li/Na}$ and $\beta_{Li/Mg}$, were increased profoundly based on their definition algorithm (Text S3), with a decreasing order of $\beta_{Li/Na}$ (68.7) > $\beta_{Li/Mg}$ (21.0) > $\beta_{Li/Pb}$ (3.6) > $\beta_{Li/Ca}$ (2.0) in the East Taijinaier Salt Lake brine (Fig. 6d).

This high $Li^+$ selectivity can be attributed to the specific recognition of $Li^+$ ion by the spinel-type λ-$MnO_2$ [66]. $Li^+$ with a small ionic radius (~0.76 Å) can be easily embedded/extracted into the 3D network structure of λ-$MnO_2$. Note that the trends in $\Gamma$ for both the synthetic and the actual brines appeared to be positively correlated with the hydrated radius of these cations except $Na^+$ ion (Table S5), implying the steric hindrance effect may play the dominant role in preferentially capturing $Li^+$ ions from brines. Such spatial site resistance makes it more difficult for ions of larger radii (e.g., $Na^+$, $Ca^{2+}$, and $Pb^{2+}$) to enter the lattice. Although $Mg^{2+}$ has a comparable radius to $Li^+$, its higher free energy of hydration makes the intercalation of $Mg^{2+}$ more thermodynamically unfavorable [65]. It has been shown that variables including pore size, surface charges of electrodes, and instinct properties of targeted ions also play a specific role in how ions can be selectively adsorbed to the porous electrodes [67]. In addition, properties such as the diffusion coefficient and hydration-free energy of $Li^+$ in water allow its preferential adsorption compared to other ions (Table S5). Therefore, it's concluded that $Li^+$ ions were thermodynamically more favorable than other ions being captured to the composite electrode as a result of a combined and complex interaction of the above variables [68]. Future work will employ techniques like EDS mapping or TOF-SIMS to directly visualize the spatial distribution of captured $Li^+$ ions within the electrode materials, providing direct evidence of the separation effect and insights into the mechanism for $Li^+$ selectivity. Combinedly, these results indicate that the NiHCF@λ-$MnO_2$ electrode demonstrates high $Li^+$ ion selectivity and great promise for $Li^+$ extraction from actual brines.

## 4. Conclusions

In summary, both NiHCF and $MnO_2$ are promising Faradaic (charge transfer) electrode candidates for electrochemical lithium ($Li^+$) extraction, allowing for high-performance recovery of the energy-critical element by structural and/or compositional tailoring and component integration. In this work, we prepared three core-shell structured NiHCF/$MnO_2$ materials (i.e., α-$MnO_2$@NiHCF, NiHCF@λ-$MnO_2$, and NiHCF@δ-$MnO_2$) based on core-shell construction strategies and comprehensively explored their $Li^+$ extraction performance on a rocking-chair capacitive deionization (RCDI) platform. Our characterization results show that both the $MnO_2$ phase and its morphology were sensitive to the synthesis conditions, with needle-like α-$MnO_2$ as the core, scale-like λ-$MnO_2$ and flower-like δ-$MnO_2$ as the shells, respectively, in the α-$MnO_2$@NiHCF, NiHCF@λ-$MnO_2$, and NiHCF@δ-$MnO_2$ composites. The electrochemical analysis results reveal that the NiHCF@λ-$MnO_2$ exhibited an excellent ion migration rate, high specific capacity, and exceptional cycling stability, followed by NiHCF@δ-$MnO_2$ and α-$MnO_2$@NiHCF. $Li^+$ extraction tests demonstrate that the NiHCF@λ-$MnO_2$ electrode showed the superior performance of $Li^+$ uptake concerning adsorption capacity, adsorption rate and energy consumption, outperforming the other two counterparts under the same conditions. The $Li^+$ adsorption capacity is potential- and feed saline-dependent, with higher cell voltages and higher saline concentrations yielding greater $Li^+$ uptake. Cycling and selectivity tests suggest that the NiHCF@λ-$MnO_2$ electrode demonstrated great cycling performance over 40 cycles of $Li^+$ extraction operation and outstanding $Li^+$ preference over other cations such as $Na^+$, $Ca^{2+}$, $Mg^{2+}$, and $Pb^{2+}$ in a synthetic brine with 10 mM of each ion, rendering a great capacity retention and remarkable separation factors. The selectivity was further evaluated in the actual brine from the East Taijinaier Salt Lake with diverse ion concentrations, and exceptional separation factors of $Li^+$ over $Na^+$ and $Mg^{2+}$ were demonstrated, respectively, showcasing the great promise of the electrode for practical application for $Li^+$ extraction. Our core-shell construction strategy appears as a viable way to integrate active electrode components for high-performance $Li^+$ extraction from brines. Further work will explore the underlying mechanism for the $Li^+$ selectivity of this composite electrode and the modulating approaches for higher electrochemical separation efficiency toward $Li^+$ from real brines.

## CRediT authorship contribution statement

**Yang Bao:** Writing – original draft, Visualization, Methodology, Investigation. **Shijun Miao:** Validation, Methodology. **Pengcheng Yin:** Validation, Investigation. **Dawei Li:** Validation, Methodology. **Feihu Li:** Writing – review & editing, Writing – original draft, Supervision, Project administration, Investigation, Conceptualization.

## Declaration of competing interest

The authors declare that they have no known competing financial interests or personal relationships that could have appeared to influence the work reported in this paper.

## Acknowledgments

The authors are grateful for the financial support from the Priority Academic Program Development (PAPD) of Jiangsu Higher Education Institutions, and to Drs. Jun Li and Mingzhe Dong at the Qinghai Institute of Salt Lakes, Chinese Academy of Sciences, for providing the East Taijinaier Salt Lake brine.

## Appendix A. Supplementary data

Supplementary data to this article can be found online at https://doi.org/10.1016/j.cej.2025.170471.

## Data availability

The data that support the findings of this study are available from the corresponding author upon reasonable request.

## References


[1] S.X. Yang, Y.G. Wang, H. Pan, P. He, H.S. Zhou, Lithium extraction from low-quality brines, Nature 636 (8042) (2024) 309–321, https://doi.org/10.1038/s41586-024-08117-1.

[2] V. Flexer, C.F. Baspineiro, C.I. Galli, Lithium recovery from brines: A vital raw material for green energies with a potential environmental impact in its mining and processing, Sci. Total Environ. 639 (2018) 1188–1204, https://doi.org/10.1016/j.scitotenv.2018.05.223.

[3] V. Balaram, M. Santosh, M. Satyanarayanan, N. Srinivas, H. Gupta, Lithium: A review of applications, occurrence, exploration, extraction, recycling, analysis, and environmental impact, Geosci. Front. 15 (5) (2024) 101868, https://doi.org/10.1016/j.gsf.2024.101868.

[4] C. Liu, Y.B. Li, D.C. Lin, P.C. Hsu, B.F. Liu, G.B. Yan, T. Wu, Y. Cui, S. Chu, Lithium extraction from seawater through pulsed electrochemical intercalation, Joule 4 (7) (2020) 1459–1469, https://doi.org/10.1016/j.joule.2020.05.017.

[5] Y.C. Xiong, J.W. Zhou, P.Y. Lu, J.W. Yin, Y.H. Wang, Z.X. Fan, Electrochemical lithium extraction from aqueous sources, Matter 5 (6) (2022) 1760–1791, https://doi.org/10.1016/j.matt.2022.04.034.

[6] M.K. Nazir, L. Dyer, B. Tadesse, B. Albijanic, N. Kashif, Lithium deportment by size of a calcined spodumene ore, Sci. Rep. 12 (1) (2022) 18335, https://doi.org/10.1038/s41598-022-22808-7.

[7] S.Y. Jiang, J.H. Zhang, K.L. Diao, X.M. Liu, Z.Z. Ding, Research advances in solvent extraction of lithium: the potential of ionic liquids, Adv. Funct. Mater. 35 (2025) 2423566, https://doi.org/10.1002/adfm.202423566.

[8] L. Baudino, C. Santos, C.F. Pirri, F. La Mantia, A. Lamberti, Recent advances in the lithium recovery from water resources: from passive to electrochemical methods, Adv. Sci. 9 (27) (2022) 2201380, https://doi.org/10.1002/advs.202201380.

[9] Z.H. Han, S.M. Qi, M.T. Fu, L. Han, C.X. Hong, Z.Y. Shen, X.C. Wang, K.Y. Su, X. G. Xue, B.W. Zhang, J.Z. Gu, H.J. Ma, A scalable route to constructing hydrogel-encapsulated lithium-ion sieves-based photothermal fabric adsorbent for solar-enhanced lithium extraction from seawater, Adv. Funct. Mater. 35 (2025) 2422901, https://doi.org/10.1002/adfm.202422901.

[10] W.T. Meng, S.F. Chen, Z.Y. Guo, F. Gao, J. Wang, J.G. Lu, Y. Hou, Q.G. He, X. L. Zhan, M. Qiu, Q.H. Zhang, Three-dimensional cationic covalent organic framework membranes for rapid and selective lithium extraction from saline water, Nat. Water 3 (2) (2025) 191–200, https://doi.org/10.1038/s44221-024-00379-3.

[11] R. Xu, X. Xiao, G. Zhang, Y.S. Ye, P. Zhang, Y.F. Yang, S.B. Shuchi, Y. Cui, Continuous lithium extraction from brine by efficient redox-couple electrodialysis, Matter 7 (11) (2024) 3876–3890, https://doi.org/10.1016/j.matt.2024.07.014.

[12] A. Battistel, M.S. Palagonia, D. Brogioli, F. La Mantia, R. Trocoli, Electrochemical methods for lithium recovery: a comprehensive and critical review, Adv. Mater. 32 (23) (2020) 1905440, https://doi.org/10.1002/adma.201905440.

[13] D.H. Lee, T. Ryu, J. Shin, J.C. Ryu, K.S. Chung, Y.H. Kim, Selective lithium recovery from aqueous solution using a modified membrane capacitive deionization system, Hydrometallurgy 173 (2017) 283–288, https://doi.org/10.1016/j.hydromet.2017.09.005.

[14] A. Siekierka, B. Tomaszewska, M. Bryjak, Lithium capturing from geothermal water by hybrid capacitive deionization, Desalination 436 (2018) 8–14, https://doi.org/10.1016/j.desal.2018.02.003.

[15] W.H. Shi, X.Y. Liu, C.Z. Ye, X.H. Cao, C.J. Gao, J.N. Shen, Efficient lithium extraction by membrane capacitive deionization incorporated with monovalent selective cation exchange membrane, Sep. Purif. Technol. 210 (2019) 885–890, https://doi.org/10.1016/j.seppur.2018.09.006.

[16] N. Xie, Y.Q. Li, Y.J. Yuan, J.M. Gong, X.L. Hu, Fabricating a flow-through hybrid capacitive deionization cell for selective recovery of lithium ions, ACS Appl. Energy Mater. 4 (11) (2021) 13036–13043, https://doi.org/10.1021/acsaem.1c02654.

[17] G.Q. Ma, J. Jiang, Y.N. Wei, A.J. Cai, L. Wang, H.J. Zhou, Lithium extraction from salt lake via rocking-chair flow electrode capacitive deionization with monovalent selective membrane, Desalination 600 (2025) 118516, https://doi.org/10.1016/j.desal.2024.118516.

[18] J.G. Zhou, Y.S. Xu, D.M. Shin, H.J. Zhou, Breaking the trade-off between capacity, stability, and selectivity for electrochemical lithium extraction via a dual-ion doping strategy, Desalination 600 (2025) 118530, https://doi.org/10.1016/j.desal.2025.118530.

[19] B. Hu, X.H. Shang, P.F. Nie, B.S. Zhang, J.M. Yang, J.Y. Liu, Lithium ion sieve modified three-dimensional graphene electrode for selective extraction of lithium by capacitive deionization, J. Colloid Interface Sci. 612 (2022) 392–400, https://doi.org/10.1016/j.jcis.2021.12.181.

[20] Y. Bao, Z.Y. Ji, H.R. Zhou, C. Zhang, S.X. Song, F.F. Jia, J.B. Li, M. Quintana, Li-ions pre-intercalation strategy of manganese oxides for capacitive deionization-based selective lithium extraction from low-grade brine, Small 21 (2025) 2406951, https://doi.org/10.1002/smll.202406951.

[21] X. Xu, Y.M. Chen, P.Y. Wan, K. Gasem, K.Y. Wang, T. He, H. Adidharma, M.H. Fan, Extraction of lithium with functionalized lithium ion-sieves, Prog. Mater. Sci. 84 (2016) 276–313, https://doi.org/10.1016/j.pmatsci.2016.09.004.

[22] D. Weng, H.Y. Duan, Y.C. Hou, J. Huo, L. Chen, F. Zhang, J.D. Wang, Introduction of manganese based lithium-ion Sieve-a review, Prog. Nat. Sci. Mater. Int. 30 (2) (2020) 139–152, https://doi.org/10.1016/j.pnsc.2020.01.017.

[23] X.Y. Zhao, Y.X. Gong, K. Gao, Y.F. Wang, H.Y. Yang, Tailored LMO@COF composite electrodes for direct electrochemical lithium extraction from high-temperature brines, Chem. Eng. J. 474 (2023) 145975, https://doi.org/10.1016/j.cej.2023.145975.

[24] X.Y. Zhao, Y.S. Wang, Y.J. Wang, H. Zhang, Z.J. Zhao, L. Zhu, Y.F. Wang, Integrating flexibility and lattice engineering in Al-Br Co-doped self-supporting $LiMn_2O_4$ electrodes for efficient lithium extraction, Chem. Eng. J. 521 (2025) 166575, https://doi.org/10.1016/j.cej.2025.166575.

[25] S. Kim, J. Lee, J.S. Kang, K. Jo, S. Kim, Y.E. Sung, J. Yoon, Lithium recovery from brine using a λ-$MnO_2$/activated carbon hybrid supercapacitor system, Chemosphere 125 (2015) 50–56, https://doi.org/10.1016/j.chemosphere.2015.01.024.

[26] Y.X. Mu, C.Y. Zhang, W. Zhang, Y.X. Wang, Electrochemical lithium recovery from brine with high Mg2+/Li+ ratio using mesoporous λ-$MnO_2$/$LiMn_2O_4$ modified 3D graphite felt electrodes, Desalination 511 (2021) 115112, https://doi.org/10.1016/j.desal.2021.115112.

[27] G.Y. Tian, M.R. Wang, K. Yao, Z.R. Ren, J. Xiang, Y.M. Xiao, L. Zhang, P.G. Cheng, J.P. Zhang, N. Tang, Quaternized poly(ether sulfone) coupled $LiMn_{1.9}Cr_{0.1}O_4$@carbon cloth for high-performance membrane capacitive li-extraction, ACS Sustain. Chem. Eng. 13 (1) (2025) 299–310, https://doi.org/10.1021/acssuschemeng.4c07073.

[28] X.H. Shang, J.Y. Liu, B. Hu, P.F. Nie, J.M. Yang, B.S. Zhang, Y.W. Wang, F. Zhan, J. S. Qiu, CNT-strung $LiMn_2O_4$ for lithium extraction with high selectivity and stability, Small Methods 6 (7) (2022) 2200508, https://doi.org/10.1002/smtd.202200508.

[29] J. Jin, Y. Bao, F.H. Li, Enhanced removal of $Cu^{2+}$ and $Pb^{2+}$ ions from wastewater via a hybrid capacitive deionization platform with $MnO_2$/N-doped mesoporous carbon nanocomposite electrodes, ACS Appl. Mater. Interfaces 17 (9) (2025) 13783–13793, https://doi.org/10.1021/acsami.4c18755.

[30] J. Jin, F. Li, $MnO_2$ decorated N-doped mesoporous carbon electrodes boost enhanced removal of $Cu^{2+}$ and $Pb^{2+}$ ions from wastewater via a hybrid capacitive deionization platform, ChemRxiv (2024), https://doi.org/10.26434/chemrxiv-2024-7j7cn.

[31] S. Zhang, Z.N. Ye, M.Y. Ma, P.C. Yin, Y. Bao, F.H. Li, Optimizing the integration of nickel hexacyanoferrate with hollow mesoporous carbon spheres (HMCSs) for highly efficient capacitive deionization, Desalination 603 (2025) 118679, https://doi.org/10.1016/j.desal.2025.118679.

[32] X.R. Cao, J. Wu, Z.H. Deng, Y. Ji, Q. Zhang, L. Guo, J.Z. Yu, G.F. Ouyang, An ultrastable RA-$LiMn_2O_4$ lithium-ion sieve for lithium extraction from brine, ACS Mater. Lett. 6 (9) (2024) 4343–4350, https://doi.org/10.1021/acsmaterialslett.4c01184.

[33] P. Srimuk, X. Su, J. Yoon, D. Aurbach, V. Presser, Charge-transfer materials for electrochemical water desalination, ion separation and the recovery of elements, Nat. Rev. Mater. 5 (7) (2020) 517–538, https://doi.org/10.1038/s41578-020-0193-1.

[34] R. Pulido, N. Naveas, J.P. Raul, T. Graber, I. Brito, J. Hernández-Montelongo, M. M. Silvan, Experimental and density functional theory study of the $Li^+$ desorption in spinel/layered lithium manganese oxide nanocomposites using HCl, Chem. Eng. J. 441 (2022) 136019, https://doi.org/10.1016/j.cej.2022.136019.

[35] H.H. Dai, R.C. Zhou, Z. Zhang, J.Y. Zhou, G.Z. Sun, Design of manganese dioxide for supercapacitors and zinc-ion batteries: similarities and differences, Energy Mater. 2 (6) (2022) 200040, https://doi.org/10.20517/energymater.2022.56.

[36] F. Wang, Y.Y. Zheng, Q.H. Chen, Z.J. Yan, D.W. Lan, E. Lester, T. Wu, A critical review of facets and defects in different $MnO_2$ crystalline phases and controlled synthesis - Its properties and applications in the energy field, Coord. Chem. Rev. 500 (2024) 215537, https://doi.org/10.1016/j.ccr.2023.215537.

[37] Y. Bao, J.X. Hao, S. Zhang, D.C. Zhu, F.H. Li, Structural/compositional-tailoring of nickel hexacyanoferrate electrodes for highly efficient capacitive deionization, Small 19 (34) (2023) 2300384, https://doi.org/10.1002/smll.202300384.

[38] P.X. Li, Y.B. Yang, E.Z. Shi, Q.C. Shen, Y.Y. Shang, S.T. Wu, J.Q. Wei, K.L. Wang, H. W. Zhu, Q. Yuan, A.Y. Cao, D.H. Wu, Core-double-shell, carbon nanotube@polypyrrole@$MnO_2$ sponge as freestanding, compressible supercapacitor electrode, ACS Appl. Mater. Interfaces 6 (7) (2014) 5228–5234, https://doi.org/10.1021/am500579c.

[39] Z.Y. Leong, H.Y. Yang, A study of $MnO_2$ with different crystalline forms for pseudocapacitive desalination, ACS Appl. Mater. Interfaces 11 (14) (2019) 13176–13184, https://doi.org/10.1021/acsami.8b20880.

[40] A.K. Das, R. Bera, A. Maitra, S.K. Karan, S. Paria, L. Halder, S.K. Si, A. Bera, B. B. Khatua, Fabrication of an advanced asymmetric supercapacitor based on a microcubical PB@$MnO_2$ hybrid and PANI/GNP composite with excellent electrochemical behaviour, J Mater. Chem. A 5 (42) (2017) 22242–22254, https://doi.org/10.1039/c7ta05134d.

[41] J. Jin, M. Li, M.T. Tang, Y. Li, Y.Y. Liu, H. Cao, F.H. Li, Phase- and crystallinity-tailorable $MnO_2$ as an electrode for highly efficient hybrid capacitive deionization (HCDI), ACS Sustain. Chem. Eng. 8 (30) (2020) 11424–11434, https://doi.org/10.1021/acssuschemeng.0c04101.

[42] K. Zhang, M. Park, L.M. Zhou, G.H. Lee, J. Shin, Z. Hu, S.L. Chou, J. Chen, Y. M. Kang, Cobalt-doped $FeS_2$ nanospheres with complete solid solubility as a high-

performance anode material for sodium-ion batteries, Angew. Chem. Int. Ed. 55 (41) (2016) 12822–12826, https://doi.org/10.1002/anie.201607469.
[43] T. Brezesinski, J. Wang, S.H. Tolbert, B. Dunn, Ordered mesoporous α-$MoO_3$ with iso-oriented nanocrystalline walls for thin-film pseudocapacitors, Nat. Mater. 9 (2) (2010) 146–151, https://doi.org/10.1038/Nmat2612.
[44] W.F. Wei, X.W. Cui, W.X. Chen, D.G. Ivey, Manganese oxide-based materials as electrochemical supercapacitor electrodes, Chem. Soc. Rev. 40 (3) (2011) 1697–1721, https://doi.org/10.1039/c0cs00127a.
[45] X.L. Yu, C.Z. Zhan, R.T. Lv, Y. Bai, Y.X. Lin, Z.H. Huang, W.C. Shen, X.P. Qiu, F. Y. Kang, Ultrahigh-rate and high-density lithium-ion capacitors through hybriding nitrogen-enriched hierarchical porous carbon cathode with prelithiated nnicrocrystalline graphite anode, Nano Energy 15 (2015) 43–53, https://doi.org/10.1016/j.nanoen.2015.03.001.
[46] M.D. Stoller, R.S. Ruoff, Best practice methods for determining an electrode material's performance for ultracapacitors, Energy Environ. Sci. 3 (9) (2010) 1294–1301, https://doi.org/10.1039/C0EE00074D.
[47] Y. Gogotsi, P. Simon, True performance metrics in electrochemical energy storage, Science 334 (6058) (2011) 917–918, https://doi.org/10.1126/science.1213003.
[48] K. Singh, Z.X. Qian, P.M. Biesheuvel, H. Zuilhof, S. Porada, L.C.P.M. de Smet, Nickel hexacyanoferrate electrodes for high mono/divalent ion-selectivity in capacitive deionization, Desalination 481 (2020) 114346, https://doi.org/10.1016/j.desal.2020.114346.
[49] A. Gong, Y.B. Zhao, M.M. He, B.L. Liang, K.X. Li, High-performance desalination of three-dimensional nitrogen-doped carbon framework reinforced Prussian blue in capacitive deionization, Desalination 505 (2021) 114997, https://doi.org/10.1016/j.desal.2021.114997.
[50] A. Majumdar, M. Haas, I. Elliot, S. Nazari, Control and control-oriented modeling of PEM water electrolyzers: a review, Int. J. Hydrog. Energy 48 (79) (2023) 30621–30641, https://doi.org/10.1016/j.ijhydene.2023.04.204.
[51] H.W. Yu, G. Naidu, C.Y. Zhang, C. Wang, A. Razmjou, D.S. Han, T. He, H. Shon, Metal-based adsorbents for lithium recovery from aqueous resources, Desalination 539 (2022) 115951, https://doi.org/10.1016/j.desal.2022.115951.
[52] Y. Wang, Q.W. Chen, Dual-layer-structured nickel hexacyanoferrate/$MnO_2$ composite as a high-energy supercapacitive material based on the complementarity and interlayer concentration enhancement effect, ACS Appl. Mater. Interfaces 6 (9) (2014) 6196–6201, https://doi.org/10.1021/am5011173.
[53] S.Y. Wang, G. Wang, Y.W. Wang, H.R. Song, S.H. Lv, T.Z. Li, C.P. Li, In situ formation of prussian blue analogue nanoparticles decorated with three-dimensional carbon nanosheet networks for superior hybrid capacitive deionization performance, ACS Appl. Mater. Interfaces 12 (39) (2020) 44049–44057, https://doi.org/10.1021/acsami.0c12421.
[54] H. Yoon, S. Jeon, T. Min, C.K. Lee, G. Lee, Pilot-scale capacitive deionization for water softening: performance, energy consumption, and ion selectivity, J. Environ. Chem. Eng. 12 (6) (2024) 114259, https://doi.org/10.1016/j.jece.2024.114259.
[55] M.A. Alkhadra, X. Su, M.E. Suss, H.H. Tian, E.N. Guyes, A.N. Shocron, K. M. Conforti, J.P. De Souza, N. Kim, M. Tedesco, K. Khoiruddin, I.G. Wenten, J. G. Santiago, T.A. Hatton, M.Z. Bazant, Electrochemical methods for water purification, ion separations, and energy conversion, Chem. Rev. 122 (16) (2022) 13547–13635, https://doi.org/10.1021/acs.chemrev.1c00396.
[56] A.C. Arulrajan, J.E. Dykstra, A. van der Wal, S. Porada, Unravelling pH changes in electrochemical desalination with capacitive deionization, Environ. Sci. Technol. 55 (20) (2021) 14165–14172, https://doi.org/10.1021/acs.est.1c04479.
[57] K. Singh, S. Porada, H.D. de Gier, P.M. Biesheuvel, L.C.P.M. de Smet, Timeline on the application of intercalation materials in capacitive deionization, Desalination 455 (2019) 115–134, https://doi.org/10.1016/j.desal.2018.12.015.
[58] E. Sebti, M.M. Besli, M. Metzger, S. Hellstrom, M.J. Schultz-Neu, J. Alvarado, J. Christensen, M. Doeff, S. Kuppan, C.V. Subban, Removal of $Na^+$ and $Ca^{2+}$ with Prussian blue analogue electrodes for brackish water desalination, Desalination 487 (2020) 114479, https://doi.org/10.1016/j.desal.2020.114479.
[59] Y.P. Zhao, M.P. Li, S.Y. Liu, M.F. Islam, Superelastic pseudocapacitors from freestanding $MnO_2$-decorated graphene-coated carbon nanotube aerogels, ACS Appl. Mater. Interfaces 9 (28) (2017) 23810–23819, https://doi.org/10.1021/acsami.7b06210.
[60] W. Xiao, H. Peng, H. Wang, Z. Bian, Impact of interfering ions on λ-$MnO_2$ for lithium recovery from brine, Sep. Purif. Technol. 365 (2025) 132657, https://doi.org/10.1016/j.seppur.2025.132657.
[61] X. Xu, Y. Zhou, Z.W. Feng, N.U. Kahn, Z.U. Khan, Y. Tang, Y.Z. Sun, P.Y. Wan, Y. M. Chen, M.H. Fan, A self-supported λ-$MnO_2$ film electrode used for electrochemical lithium recovery from brines, ChemPlusChem 83 (6) (2018) 521–528, https://doi.org/10.1002/cplu.201800185.
[62] M.J. Zhang, C. Sun, J.Y. Li, C.L. Shi, X.M. Li, B. Zhao, Suppressed Mn dissolution behavior to improve cycling performance of Cr-modified $Li_{1-x}Mn_2O_4$ electrodes, Colloids Surf. A: Physicochem. Eng. Asp. 710 (2025) 136283, https://doi.org/10.1016/j.colsurfa.2025.136283.
[63] F.E. Ahmed, A. Khalil, N. Hilal, Emerging desalination technologies: current status, challenges and future trends, Desalination 517 (2021) 115183, https://doi.org/10.1016/j.desal.2021.115183.
[64] R. Chitrakar, H. Kanoh, Y. Miyai, K. Ooi, A new type of manganese oxide ($MnO_2$•$0.5H_2O$) derived from $Li_{1.6}Mn_{1.6}O_4$ and its lithium ion-sieve properties, Chem. Mater. 12 (10) (2000) 3151–3157, https://doi.org/10.1021/cm0000191.
[65] J.G. Gamaethiralalage, K. Singh, S. Sahin, J. Yoon, M. Elimelech, M.E. Suss, P. Liang, P.M. Biesheuvel, R.L. Zornitta, L.C.P.M. de Smet, Recent advances in ion selectivity with capacitive deionization, Energy Environ. Sci. 14 (3) (2021) 1095–1120, https://doi.org/10.1039/d0ee03145c.
[66] D.H. Snydacker, V.I. Hegde, M. Aykol, C. Wolverton, Computational discovery of Li-M-O Ion exchange materials for lithium extraction from brines, Chem. Mater. 30 (20) (2018) 6961–6968, https://doi.org/10.1021/acs.chemmater.7b03509.
[67] R.L. Chen, J.Y. Feng, J. Jeon, T. Sheehan, C. Ruttiger, M. Gallei, D. Shukla, X. Su, Structure and potential-dependent selectivity in redox-metallopolymers: electrochemically mediated multicomponent metal separations, Adv. Funct. Mater. 31 (15) (2021) 2009307, https://doi.org/10.1002/adfm.202009307.
[68] Z. Li, C.Y. Li, X.W. Liu, L. Cao, P.P. Li, R.C. Wei, X. Li, D. Guo, K.W. Huang, Z.P. Lai, Continuous electrical pumping membrane process for seawater lithium mining, Energy Environ. Sci. 14 (5) (2021) 3152–3159, https://doi.org/10.1039/d1ee00354b.